Microlensing makes lensed quasar time delays significantly time variable

S. S. Tie[1][⋆] and C. S. Kochanek[1,2]

[1]*Department of Astronomy, The Ohio State University, 140 West 18th Avenue, Columbus, OH 43210, USA*
[2]*Center for Cosmology and AstroParticle Physics, The Ohio State University, 191 W. Woodruff Avenue, Columbus, OH 43210, USA*

ABSTRACT

The time delays of gravitationally lensed quasars are generally believed to be unique numbers whose measurement is limited only by the quality of the light curves and the models for the contaminating contribution of gravitational microlensing to the light curves. This belief is incorrect – gravitational microlensing also produces changes in the actual time delays on the ∼day(s) light-crossing time-scale of the emission region. This is due to a combination of the inclination of the disc relative to the line of sight and the differential magnification of the temperature fluctuations producing the variability. We demonstrate this both mathematically and with direct calculations using microlensing magnification patterns. Measuring these delay fluctuations can provide a physical scale for microlensing observations, removing the need for priors on either the microlens masses or the component velocities. That time delays in lensed quasars are themselves time variable likely explains why repeated delay measurements of individual lensed quasars appear to vary by more than their estimated uncertainties. This effect is also a new important systematic problem for attempts to use time delays in lensed quasars for cosmology or to detect substructures (satellites) in lens galaxies.

Key words: quasars: general – cosmological parameters – cosmology: observations.

1 INTRODUCTION

Ever since Refsdal (1964) proposed the method, there have been hopes that gravitational lens time delays can be used to constrain the cosmological model (see the review by Treu & Marshall 2016). Current studies are quite optimistic, with Bonvin et al. (2017), based also on Fassnacht et al. (2002), Suyu et al. (2010), Tewes et al. (2013b) and Suyu et al. (2014), claiming a 3.8 per cent measurement of (effectively) H_0 based on time delay measurements in three lenses. Fundamentally, time delays constrain $\Delta t \propto H_0^{-1}(1 - \langle\kappa\rangle)$ where $\langle\kappa\rangle$ is the mean surface density (convergence) in the annulus between the two images (Kochanek 2002). The surface density $\langle\kappa\rangle$ must be constrained with some additional information about the geometry or kinematics of the lens (see the review by Kochanek 2006). One contribution to $\langle\kappa\rangle$ is simply the random fluctuations in the density along the line of sight (LOS) to the lens (see, e.g. Keeton & Zaludoff 2004; Greene et al. 2013; McCully et al. 2017), and the other is the internal structure of the lens galaxy (see the discussion in Kochanek 2006).

The essence of the programme to use lenses to constrain cosmology is to obtain time delays of *N* lenses with individual time delay, LOS convergence and lens surface density uncertainties of σ_t, σ_{los} and $\sigma_{\langle\kappa\rangle}$ and then combine them to obtain a fractional error in H_0 (really the combination of cosmological distances entering the lens time delay) of $\sigma_H^2/H_0^2 \sim (\sigma_{\delta t}^2/\delta t^2 + \sigma_{los}^2 + \sigma_{\langle\kappa\rangle}^2)/N$. It is generally assumed that the first two terms in this error budget are dominated by random errors and their contributions to the overall error will scale as $N^{-1/2}$. There are far greater concerns about whether the last term may already be dominated by systematic errors (e.g. Schneider & Sluse 2013; Birrer, Amara & Refregier 2016) for which there is no benefit from combining lenses. In any case, any ultimate claim of achieving $\sigma_H/H_0 \simeq 0.01$ is equivalent to the claim that there are also no systematic errors in the surface density $\langle\kappa\rangle$ estimates at a comparable level. It will be challenging to prove this assertion.

This is not, however, the focus of this paper. Our concern here is the accuracy of the time delay measurements – the error contribution from $\sigma_{\delta t}/\delta t$. Dating from the attempts to measure gravitational lens time delays in the very first lens, Q 0957+561 (Walsh, Carswell & Weymann 1979), time delay measurements have produced controversy (e.g. Schild 1990 versus Press, Rybicki & Hewitt 1992, resolved in favour of the former by Kundić et al. 1997). In most modern studies, the question is not so much the basic validity of the delay but the accuracy of the uncertainty estimates, and there have recently been a series of tests and comparisons of various delay measurement methods (e.g. Tewes, Courbin & Meylan 2013a; Dobler et al. 2015; Liao et al. 2015; Bonvin et al. 2016, 2017). An adequate summary of these studies is that with reasonably good light curves, it is feasible to measure time delays with both high accuracy and precision.

All of these studies assume, however, that the measured time delay is the standard cosmological delay used in all lens models.

⋆ E-mail: tie.5@osu.edu

They also assume that the ratios of delays depend only on the large-scale potential of the lens galaxy (possibly with some effects from the largest substructures in the galaxy; Keeton & Moustakas 2009). In this paper, we show that for gravitationally lensed quasars, microlensing by the stars in the lens galaxy (see the review by Wambsganss 2006) makes both of these assumptions incorrect.

Microlensing changes time delays on the scale of the light-crossing time of the accretion disc, which has a typical scale of light days. These microlensing-induced time delays will then slowly change as the accretion disc moves relative to the stars doing the microlensing.

There are two causes of the microlensing effect on time delays. The first is very simple. If the accretion disc does not lie in the plane of the sky, different parts of the disc lie at different LOS distances. This has a negligible consequence based on the normal expression for the time delay, as partially discussed in Yonehara (1999), Goicoechea (2002) and in more detail below. However, the normal time delay expression neglects the variations in the delay due to the actual change in the LOS distance Δz to the source (because this term has been subtracted). This missing term is a delay of order $(1 + z_s)\Delta z/c$ where $\Delta z/c$ is the proper light travel time and $1 + z_s$ is the effect of time dilation from the source redshift z_s. Without microlensing, this effect is unimportant because $\langle \Delta z \rangle$ is the same for all images. However, microlensing, by its very definition, differentially magnifies different regions of the disc and $\langle \Delta z \rangle$ will vary between images when weighted by the spatially varying microlensing magnification.

The second effect is more subtle and exists even for a face-on disc. The variability of the disc is due to a pattern of temperature fluctuations on the disc with the observed light curve representing an average of the fluctuations. The simplest case to explain is a 'lamp post' model, where luminosity fluctuations $\delta L(t)$ close to the disc centre illuminate the disc to drive the temperature fluctuations but with a lag due to the light travel time from the centre, $\delta T(R, t) \sim \delta L(t - R/c)$ (Krolik et al. 1991). The lamp post model assumes that the variability of the UV/optical emission by the disc is driven by reprocessing of the variable X-ray emission produced near the central black hole (see, e.g. Wanders et al. 1997; Collier et al. 1998). While there is no guarantee that the lamp post model explains all quasar variability (see, e.g. Dexter & Agol 2011), it has been successfully used to model the wavelength-dependent ultraviolet/optical/near-IR variability of NGC 2617 (Shappee et al. 2014) and NGC 5548 (Starkey et al. 2017). The blackbody function is quite broad, so a broad range of disc radii contribute to the variability observed at any given wavelength. Microlensing differentially weights the emission from the disc, so the mean emission radius of a microlensed disc is different from that of the unmicrolensed disc or a differently microlensed image of the same disc. This both introduces differential time delays on the scale of the light-crossing time and means that the light curves of lensed images will not be identical even for a fixed microlensing magnification pattern. There has been some prior discussion of this latter point (e.g. Gould & Miralda-Escudé 1997; Wyithe & Loeb 2002; Dexter & Agol 2011), largely to explain the rapid, uncorrelated variability seen in the light curves of some lensed quasars (e.g. Burud et al. 2002; Schechter et al. 2003). While we will illustrate this effect using the 'lamp post' model, the effect will be present for any model of quasar variability.

To summarize, we should expect gravitational lens time delays to be affected by microlensing, with image-to-image shifts on the time-scale of the light-crossing time of the disc – days. In Section 2, we work through the basic mathematics of the effects. In Section 3, we explore several numerical examples based on two of the lensed quasars used in Bonvin et al. (2017), RXJ 1131−1231 (Sluse et al. 2003) and HE 0435−1223 (Wisotzki et al. 2002). We summarize the consequences of our results in Section 4.

2 MATHEMATICS

The standard expression for the time delay of a lens is

$$\tau_{std} = \frac{D_{OL}D_{OS}}{cD_{LS}} \left[\frac{1}{2}(\boldsymbol{\theta} - \boldsymbol{\beta})^2 - \phi(\boldsymbol{\theta}) \right], \tag{1}$$

where $\boldsymbol{\theta}$ and $\boldsymbol{\beta}$ are the angular position of the image and the source and $\phi(\boldsymbol{\theta}) = (D_{LS}/D_{OS})\phi_0(\boldsymbol{\theta})$ is the projected lensing potential (e.g. Schneider 1985; Blandford & Narayan 1986). The distances are proper motion distances between the observer, lens and source. For a flat universe, they are simply the comoving distances and $D_{OS} = D_{OL} + D_{LS}$. Using these distances instead of angular diameter distances, both allow the use of this simple relation and eliminates extra redshift factors[1]. The lens potential combines a function $\phi_0(\boldsymbol{\theta})$ which is independent of the source distance with a source distance scaling of D_{LS}/D_{OS} for all models. Using Fermat's principle, the observed images are located at solutions of $\nabla_\theta \tau_{std} = 0$.

Now consider a second source displaced in angle to $\boldsymbol{\beta} + \delta\boldsymbol{\beta}$ and source redshift to $z_s + \delta z_s$. The images of this source will have different time delays due to the shift in the source position and the change in the *Einstein* radius of the lens. If we define $F = D_{OS}/D_{LS}$, the change in the delay for any two associated images is

$$\Delta\tau_{std} = \frac{D_{OL}D_{OS}}{cD_{LS}} \left[\delta\boldsymbol{\beta} \cdot (\boldsymbol{\beta} - \boldsymbol{\theta}) + \frac{1}{2}\frac{\delta z_s}{F}\frac{dF}{dz_s}(\boldsymbol{\beta} - \boldsymbol{\theta})^2 \right], \tag{2}$$

where the first term is the one previously discussed by Yonehara (1999) and Goicoechea (2002). The overall delays have a general scale of $(D_{OL}D_{OS}/cD_{LS})\Delta\theta^2$, where $\Delta\theta^2$ is the image separation (see, e.g. the review by Kochanek 2006). This means that the fractional change in the time delay from the first term is of order $|\delta\beta/\Delta\theta| \sim 10^{-5}$ for a disc scale of order 10 light days and a lens *Einstein* radius of order a 1 kpc. Hence, as fully realized by Yonehara (1999) and Goicoechea (2002), this effect only matters for sources separated by distances that are a non-trivial fraction of 1 kpc. The second term was not considered in these papers and produces a fractional correction of order $|(\delta z_s/F)(dF/dz_s)|$. For a flat universe where $D = (c/H_0)\int dz/E(z)$ with $E(z) = H(z)/H_0$, this becomes $(c\delta z_s/H(z_s)D_{OS})(D_{OL}/D_{LS})$ where the first term is essentially the fractional change in the distance to the source, which is $\sim 10^{-12}$ and so even less important than the first term. At this point, the reader may be wondering why this paper is being written.

We have, however, left out an important effect. Equation (1) is the time delay relative to a fiducial ray from the observer to the source along the optic axis. The actual total delay is not τ_{std} but (for a flat universe)

$$\tau = \frac{D_{OS}}{c} + \tau_{std}. \tag{3}$$

For the time delay between two sources at a common distance, the first term simply cancels and thus is simply removed as a nuisance parameter to derive equation (1). For two sources at different distances, however, it produces a delay difference of $(1 + z_s)\Delta z/c$ where Δz is the proper separation of the two sources at the source and the net delay is simply the lag in the rest frame of the source time-dilated by the source redshift. Unlike the two terms that result

---

[1] This is true of most lensing calculations, see Kochanek (1993).

from shifting the source in equation (1), this term has the scale of the source size and it will matter for time delays between two images if the light contributing to the first image has an average source distance different from that contributing to the second image.

To calculate the delay shifts created by the inclination of the disc, we require a disc model. Since we also want to compute the second effect created by differential microlensing of the variable flux, it should also allow for a simple model of the variable flux. We will consider a standard, non-relativistic, thin disc model emitting as a blackbody (Shakura & Sunyaev 1973). If we are observing at wavelength rest λ, it is useful to define

$$\xi = \frac{hc}{kT_0(R)\lambda} = \left(\frac{R}{R_0}\right)^{3/4}\left(1 - \sqrt{\frac{R_{\rm in}}{R}}\right)^{-1/4}, \quad (4)$$

where $R > R_{\rm in}$, $T_0(R)^4 \propto R^{-3}(1 - \sqrt{R_{\rm in}/R})$ is the temperature profile of the disc,

$$R_0 = \left[\frac{45\,G\lambda_{\rm rest}^4 M_{\rm BH}\dot{M}}{16\pi^6 h_{\rm p}c^2}\right]^{1/3}$$

$$= 9.7 \times 10^{15}\left(\frac{\lambda_{\rm rest}}{\mu m}\right)^{4/3}\left(\frac{M_{\rm BH}}{10^9\,{\rm M}_\odot}\right)^{2/3}\left(\frac{L}{\eta L_{\rm E}}\right)^{1/3}\,{\rm cm} \quad (5)$$

is the radius where the disc temperature matches the photon wavelength, $kT = h_{\rm p}c/\lambda_{\rm rest}$, and $R_{\rm in} = \alpha GM_{\rm BH}/c^2$ is the inner edge of the disc (e.g. Morgan et al. 2010). Here, $h_{\rm p}$ is the Planck constant, k is the Boltzmann constant, $M_{\rm BH}$ is the black hole mass, $\dot{M}$ is the mass accretion rate, $L/L_{\rm E}$ is luminosity in units of the Eddington luminosity, $\eta = L/\dot{M}c^2$ is the accretion efficiency and $\alpha = 6$ for a Schwarzschild black hole and $\alpha = 1$ for a corotating equatorial orbit around a Kerr black hole. Converted to a time-scale and using the observed wavelength instead of the rest wavelength,

$$\frac{(1 + z_{\rm s})R_0}{c} \simeq \frac{3.8\,{\rm d}}{(1 + z_{\rm s})^{1/3}}\left(\frac{\lambda_{\rm obs}}{\mu m}\right)^{4/3}\left(\frac{M_{\rm BH}}{10^9\,{\rm M}_\odot}\right)^{2/3}\left(\frac{L}{\eta L_{\rm E}}\right)^{1/3}. \quad (6)$$

The unperturbed surface brightness profile of the disc is simply

$$I_0(R) \propto \left[\exp(\xi) - 1\right]^{-1}. \quad (7)$$

Ignoring the inner edge of the disc ($R_{\rm in} \to 0$), the mean radius of the unperturbed surface brightness profile is $\langle RI_0\rangle/\langle I_0\rangle = 3.36R_0$. That we are using a monochromatic wavelength is unimportant, as the radial width due to the blackbody emission is significantly more important than the wavelength spread from a typical broad-band filter.

In the simplest 'lamp post' model of variability (e.g. Cackett, Horne & Winkler 2007), the fractional temperature variation is independent of radius in the disc, so

$$T(R, t) = T_0(R)\left[1 + f(t - R/c)\right], \quad (8)$$

where $T_0(R)$ is the unperturbed temperature profile and $f(t - R/c)$ is the fractional luminosity variability 'lagged' by the light travel time R/c from the disc centre. If we assume the temperature variations are small, then we can Taylor expand the blackbody function to find that the time-variable emission is

$$\delta I(R, t) \propto f(t - R/c)G(\xi) \quad \text{where} \quad G(\xi) = \frac{\xi\exp(\xi)}{(\exp(\xi) - 1)^2} \quad (9)$$

comes from the temperature derivative of the blackbody and the definition of f. The average radius of the variable flux, $\langle RG\rangle/\langle G\rangle = 5.04R_0$, is larger than that of the unperturbed disc because a constant fractional temperature fluctuation produces larger surface brightness fluctuations at larger radii where the disc becomes cooler.

We can characterize the effects of microlensing by averaging the delays over the variable surface brightness $G(\xi)$ weighted by the absolute value of the microlensing magnification $M(u, v)$. Let the disc be tilted relative to the LOS by an inclination angle i with $i = 0$ corresponding to the disc lying in the plane of the sky. If a point in the disc is labelled by $(x, y, z) = R(\cos\theta, \sin\theta, 0)$ and we rotate about the y-axis, then the observed position is $(u, v, w) = R(\cos\theta\cos i, \sin\theta, -\cos\theta\sin i)$. The average delay between the driving source $f(t)$ and the observer is

$$\langle\delta t\rangle = \frac{1 + z_{\rm s}}{c}\frac{\int du dv G(\xi)M(u, v)R(1 - \cos\theta\sin i)}{\int du dv G(\xi)M(u, v)}, \quad (10)$$

where $u = R\cos\theta\cos i$ and $v = R\sin\theta$ are coordinates on the reference source plane of the lens, and $R^2 = u^2/\cos^2 i + v^2$. The factor governing the mean delay $R(1 - \cos\theta\sin i)/c$ combines the propagation delay R/c for the lamp post, with the LOS delay $(R/c)\cos\theta\sin i$ due to the inclination of the disc. Without microlensing [$M(u, v) \equiv 1$] and ignoring the inner disc edge, the inclination of the disc has no effects and we just measure the mean lag between the driving perturbation and the observed light curve, $\langle\delta t\rangle = 5.04(1 + z_{\rm s})R_0/c$.

It is relatively easy to show that the primary lens potential and its satellites cannot produce large enough magnification gradients across the accretion disc to produce an observable effect. This is not true of microlensing of the disc by the stars near each lensed image. The basic physics of the effect, that the star field near each image produces a different and time variable magnification of the accretion disc, means that there are gradients in the magnification on the physical scale of the disc and that the characteristic amplitude of the microlensing-induced delays must be of order the light-crossing time of the disc.

Fig. 1 shows the two contributions to the mean delay in equation (10) for a linear fold caustic parallel to the v-axis as a function of its position u_0 as it is moved across the disc. The magnification produced by the fold caustic is $M = A|u - u_0|^{-1/2}$ for $u \geq u_0$ and 0 for $u < u_0$. For the R/c term of the delay, we have subtracted the lag in the absence of microlensing in order to focus on the changes created by the effect. Since the fold is moving along the projected short axis of the disc, the fold position is scaled by the projected short axis disc scalelength, $u_0/R_0\cos i$. The scale of the delays is $(1 + z_{\rm s})R_0/c$, with the term due to the lag in the lamp post model (R/c) being independent of the inclination, and the term due to the disc inclination ($R\cos\theta\sin i$) depending on the inclination. We have set $R_{\rm in} = R_0/100$, although the results are insensitive to this choice for the parameter ranges relevant to optical monitoring of lensed quasars. For our definitions, the near side of the disc has $u < 0$ and the far side has $u > 0$.

We can qualitatively understand the behaviour of both terms. Consider the term due to the inclination of the disc first. When u_0 is negative, the caustic lies on the near side of the disc and so magnifies parts of the disc with shorter, negative delays. However, the fold magnification is not very singular, and so at large distances the dropping flux of the disc matters more than the magnification and the average delay becomes that of an unmicrolensed disc. As the caustic approaches the disc centre, the magnification of the near side makes the lag increasingly negative, but not by huge factors. The sign reverses before the caustic reaches the disc centre because the total flux from the far side now exceeds that from the near side. Once the caustic passes the disc centre, the lag simply increases because there is no longer any contribution from the near side of
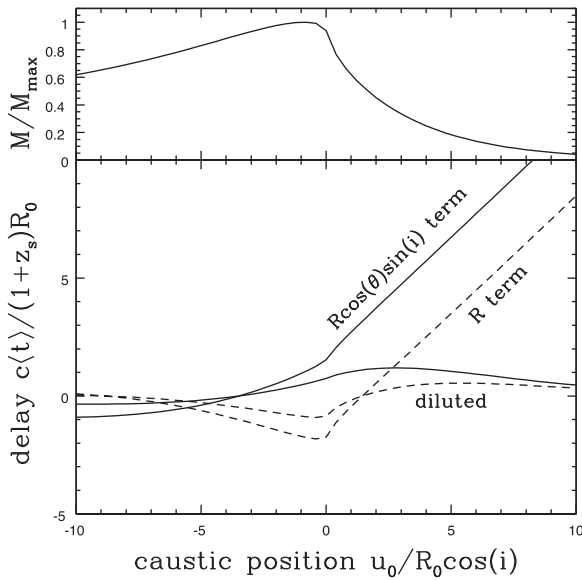
Figure 1. The observed mean time delay $\langle t \rangle$ in units of $(1 + z_s)R_0/c$ (lower panel) and magnification relative to peak M/M_{max} (top panel) for a linear fold caustic moving across a disc. The caustic is oriented parallel to the long axis of the disc and its position $u_0/R_0 \cos i$ is in units of the projected, short axis of the disc with the disc centre at the origin. The solid line shows the inclination-dependent term ($R \cos \theta \sin i$) and the dashed line shows the inclination-independent term (R). The lower amplitude 'diluted' curves show the effect of adding flux equal to that produced by the caustic at its peak and with no lag.

the disc or smaller radii than the distance of the caustic from the disc centre.

The term due to the lamp post model has some qualitative differences. It is again negligible when the caustic is on the near side and at large radius, but slightly positive because it is enhancing the contribution from large radii. As the caustic approaches the disc centre, it produces a negative mean lag by enhancing the contribution from small radii. Then, as it moves outwards, it also produces an increasingly positive lag for the same reasons as the inclination-dependent term.

The flux from a microlensed quasar is never due to a single fold caustic. It is the sum of the flux from the direct image plus some number of additional image pairs created by microlensing (see, e.g. Granot, Schechter & Wambsganss 2003). The model with a single fold caustic explores the contribution of a single image pair created by a fold caustic, which must then be combined with the fluxes of all the other images. When the flux from this image pair is small compared to the flux of the other images, the observed delay will be dominated by the delays associated with the other images. Fig. 1 also shows the magnification produced by the caustic relative to its peak, M/M_{max}. The magnification rises until the caustic approaches the disc centre and then declines. Thus, when the caustic is producing the largest shift in the time delay, it is also making a smaller and smaller contribution to the observed flux because only the outer parts of the disc are being lensed by the fold caustic.

We can get a sense of the consequences by assuming that there is additional flux equal to the flux produced by the caustic at its peak and with an average lag of zero. Under these assumptions, the mean lag becomes $\langle \delta t \rangle M/(M + M_{max})$, which is also shown in Fig. 1. The dilution by the additional flux eliminates the divergence in the delay as the caustic moves out to increasingly large radii. Reality is

more complex, which is why numerical simulations are ultimately required to understand the magnitude of the effect.

3 NUMERICAL SIMULATIONS

We demonstrate the effects of microlensing on gravitational lens time delays using numerical simulations for two of the lensed quasars, RXJ 1131−1231 and HE 0435−1223, used by Suyu et al. (2014) and Bonvin et al. (2017) to constrain H_0. RXJ 1131−1231 is a four-image lensed quasar with $z_s = 0.658$ and $z_l = 0.295$ (Sluse et al. 2003). Based on the H β line width from Sluse et al. (2003), Dai et al. (2010) estimated the black hole mass to be $(1.3 \pm 0.3) \times 10^8$ M$_\odot$. HE 0435−1223 is another four-image lensed quasar with $z_s = 1.689$, $z_l = 0.46$ and an estimated black hole mass of 0.5×10^9 M$_\odot$ (see Mosquera & Kochanek 2011 and references therein). Based on equation (5), the accretion disc sizes for RXJ 1131−1231 and HE 0435−1223 are $R_0 = 7.34 \times 10^{14}$ cm (0.28 light days) and $R_0 = 9.37 \times 10^{14}$ cm (0.36 light days), respectively, in the observed R band (6586 Å) for an Eddington ratio of $L/L_E = 0.1$ and a radiative efficiency of $\eta = 0.1$.

We created magnification maps for each lensed image using the ray-shooting method described in Kochanek (2004). The microlensing parameters, given in Table 1, correspond to a macro model with a stellar mass fraction of 0.2 relative to a pure de Vaucouleurs' model (Dai et al. 2010). The magnification maps have dimensions of 8192×8192, an outer scale of $20\langle R_e \rangle$ and a pixel scale of $0.00244 \langle R_e \rangle$, where $\langle R_e \rangle$ is the *Einstein* radius at the source plane. We assume a mean microlens mass of $\langle M/M_\odot \rangle = 0.3$ for both lenses, leading to an outer scale of 5.02×10^{17} cm and a pixel scale of 6.12×10^{13} cm for RXJ 1131−1231 and an outer scale of 5.89×10^{17} cm and a pixel scale of 7.19×10^{13} cm for HE 0435−1223. The accretion disc scalelengths R_0 are ~12 times the pixel scale, while the region dominating the variability (~$5R_0$) is ~60 times the pixel scale. Figs 2 and 3 show the full 8192×8192 magnification patterns for image A of each lens. All magnification patterns have a mean magnification of unity.

We calculated the mean delays between the driving source (the 'lamp post') and the observer using equation (10) for each lensed image, where the surface brightness $G(\xi)$ is given by equation (9) and the inner edge of the disc is (safely) ignored. We investigated four disc configurations with inclination i and position PA angles of (i) $i = 30°$, PA $= 0°$, (ii) $i = 30°$, PA $= 45°$, (iii) $i = 30°$, PA $= 90°$ and (iv) $i = 0°$. The position angles determine whether the long axis of the tilted disc is parallel, perpendicular, or at an angle to the caustic structures in the magnification maps. In this paper, the long axis of the tilted disc is perpendicular (parallel) to the caustic structures for PA $= 0°$ (PA $= 90°$). Note that the last case (iv) corresponds to a face-on disc where the position angle does not
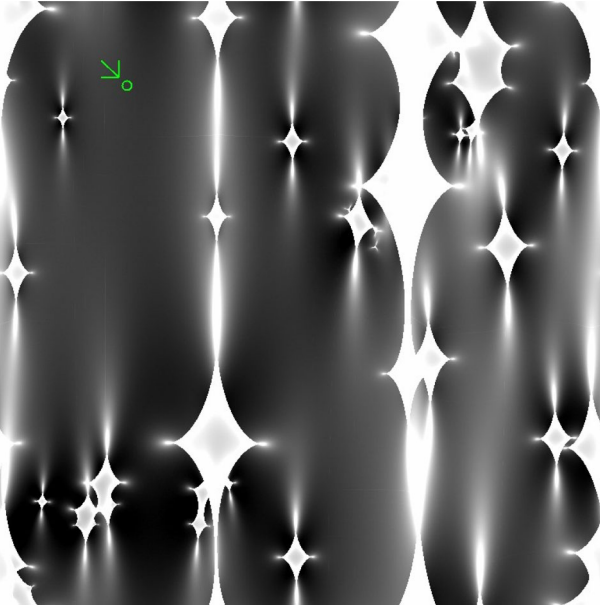
Table 1. Microlensing model parameters.

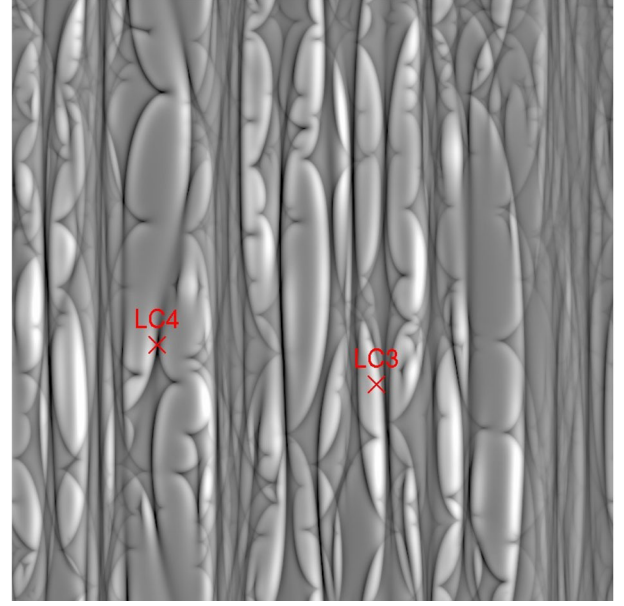| Lens	Image	κ	γ	κ_*/κ
RXJ 1131−1231	A	0.618	0.412	0.0667
	B	0.581	0.367	0.0597
	C	0.595	0.346	0.0622
	D	1.041	0.631	0.1590
HE 0435−1223	A	0.604	0.262	0.0500
	B	0.734	0.395	0.0801
	C	0.605	0.265	0.0500
	D	0.783	0.427	0.0930
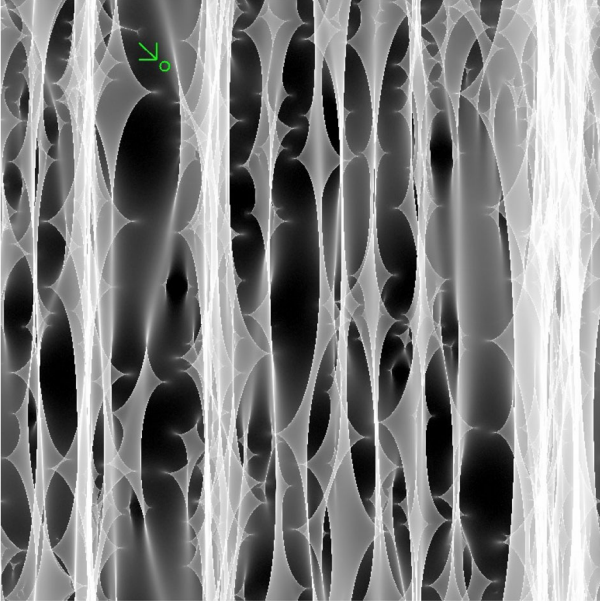
Figure 2. Magnification pattern for image A of RXJ 1131−1231. The magnification increases from darker/de-magnified to brighter/magnified regions. The green circle on the upper left shows the mean radius of the variability-dominated region, ∼$5R_0$. The pattern spans $20\langle R_e \rangle$.


Figure 4. Delay map for image A of RXJ 1131−1231, where the disc is inclined to $i = 30°$ and rotated to PA $= 45°$ for the source size R_0. The mean delays span from −1.35 d to +3.91 d and increase from the dark to the bright regions, with black indicating negative delays. The red crosses mark the points used for the light curves LC3 and LC4 in Fig. 10.

Figure 3. Magnification pattern for image A of HE 0435−1223. The format is the same as for Fig. 2.
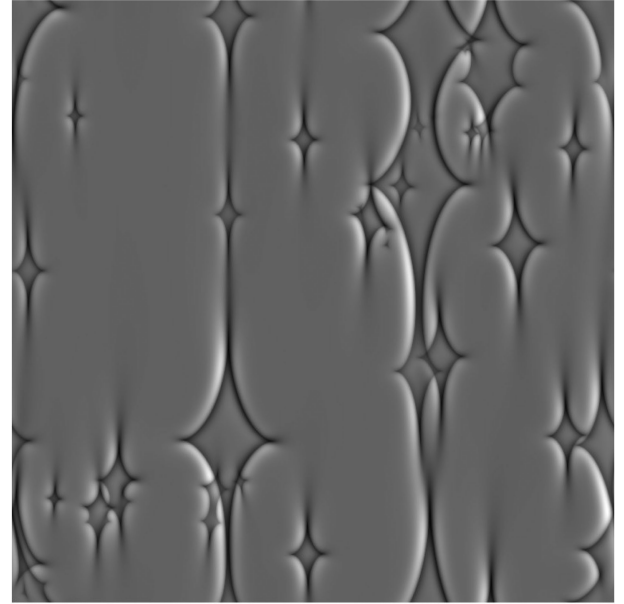
Figure 5. Delay map for image A of HE 0435−1223 using the same disc configuration as in Fig. 4. The mean delays span −2.27 d to +2.59 d and increase from dark to bright regions, with negative delays shown in black.

matter. For each disc configuration, we also investigated the effect of decreasing and increasing the source size by a factor of 2.

Examples of mean delay maps for image A of the two lenses are shown in Figs 4 and 5, where the constant delay $\langle \delta t \rangle = 5.04(1 + z_s)R_0/c$ of the lamp post model has been subtracted. The maps represent time delay perturbations due to microlensing, typically on the order of ∼ a day, with both positive and negative delays. The negative delays are shown in black, while the positive delays increase from darker to brighter regions. The edges and structures where the time delays change rapidly and frequently flip signs are due to caustics in the corresponding magnification

patterns, shown in Figs 2 and 3. The delay maps for all four disc configurations and our standard range of source sizes are shown in Fig. 6 for image A of RXJ 1131−1231. Note how the delay shifts become larger as the long axis of the disc becomes parallel to the caustic network. Similarly, the effect becomes larger as the disc becomes larger.

Figs 7–9 show the mean delay distributions for the different disc configurations for all images of the lenses, based on ∼300 000 randomly selected points from their delay maps. There are several
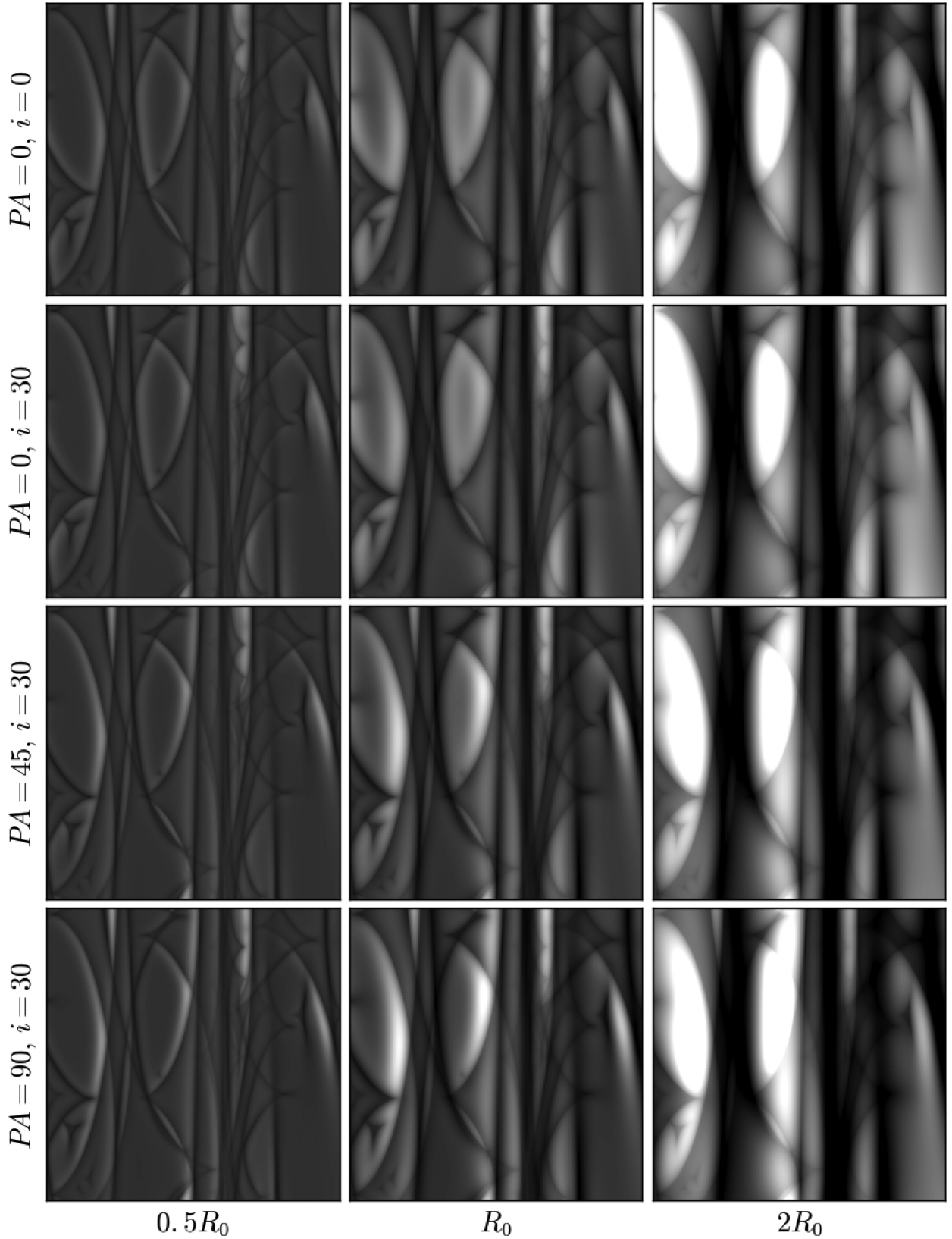
Figure 6. Magnified views of the delay maps for image A of RXJ 1131−1231 at various disc configurations. The top row is for a face-on disc and the lower three rows are for a disc inclined by $i = 30°$ with position angles of PA = 0°, 45° and 90°, respectively. Each column refers to a different source size: (left) $0.5R_0$, (middle) R_0 and (right) $2R_0$. All images are on the same scale with the minimum set at −1 d and maximum at +3 d, although certain pixels have delays that fall outside of this range. Similar to Figs 4 and 5, black is used for negative delays and white for positive delays.
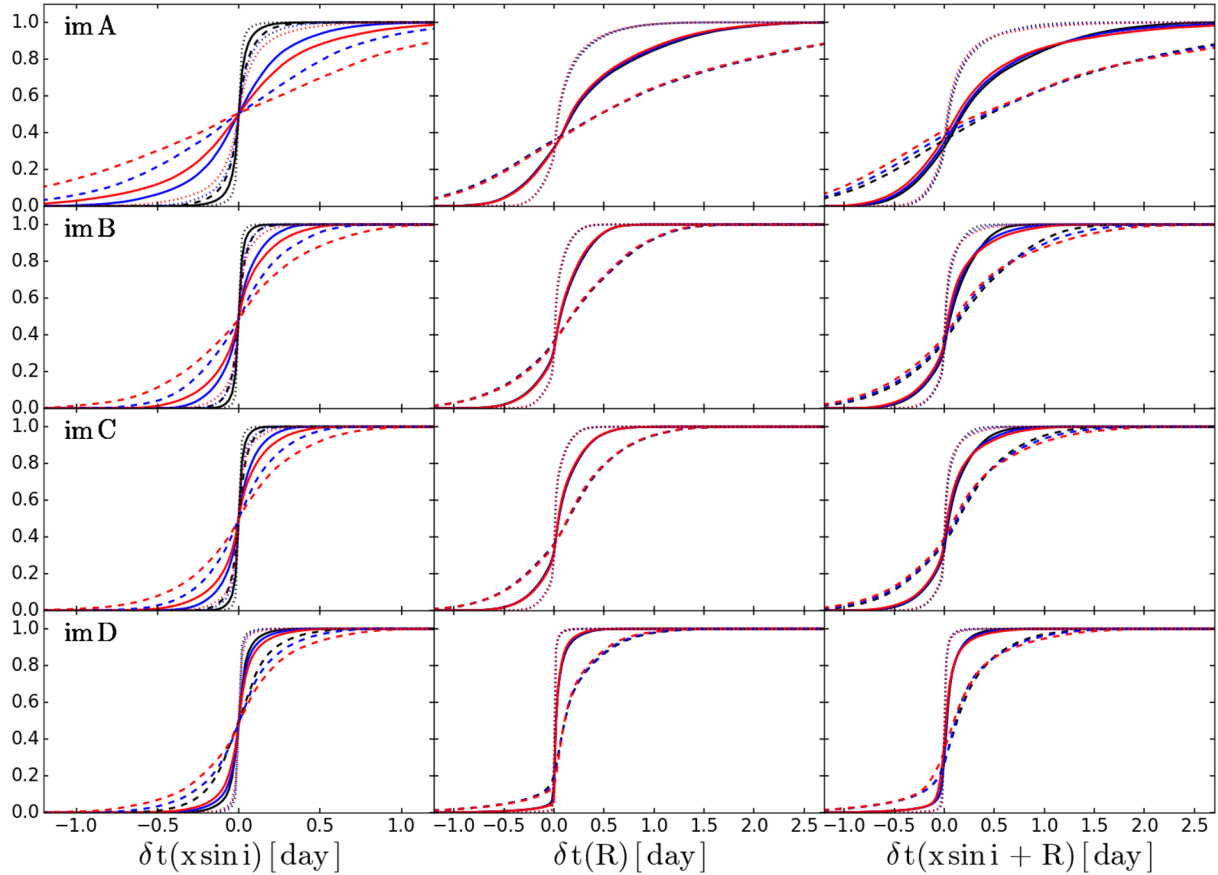
Figure 7. Cumulative distributions of the microlensing-induced mean delays for RXJ 1131−1231 when the disc is inclined to $i = 30°$. The row refers to the different lensed images while the column refers to the different delay contributions: from left to right, the delay component from the LOS inclination term, the R/c term and their combination. The different colours indicate different disc position angles: black for PA $= 0°$, blue for PA $= 45°$ and red for PA $= 90°$. The different line styles refer to the different source sizes: R_0 as the solid line, $2R_0$ as the dashed line and $0.5R_0$ as the dotted line.

interesting points to note from the delay distributions. First, the LOS delays from the disc inclination have a zero mean and are symmetric about zero delay, as expected. On the other hand, the R/c delays depend little on inclination and have a positive mean. The skew to positive delays can be understood as follows. Producing a negative lag for the R/c term requires magnifying only the inner part of the disc, which rarely happens because the caustic structures generally have scales larger than $\sim 5R_0$ and will magnify the outer parts of the disc as well. On the other hand, it is relatively easy to magnify the outer parts of the disc without magnifying the inner parts, leading to the delay asymmetry. Each image therefore has a non-zero mean for the total delay.

For all source sizes, the magnitudes of the total delays increase from a PA of $0°$ (perpendicular to caustic structures) to a PA of $90°$ (parallel to caustic structures). This is because when the long axis of the disc is perpendicular to the caustic structures, regions of positive and negative LOS delays are being magnified at the same time, leading to a smaller overall effect. When the caustic structures are parallel to the long axis of the disc, it is easier to magnify regions with only one sign of the delay. Therefore, microlensing has a more significant effect when the long axis of the disc is parallel to the caustic structures. Like the disc inclination, the disc PA has a larger effect on the LOS delays than the R/c delays. The overall delays are also larger for a larger source size and smaller for a smaller source. Even when the disc is face-on, there are still non-negligible microlensing delay contributions due to the light travel time from

the lamp post to the disc. In all cases, we have subtracted the mean delay $\langle \delta t \rangle = 5.04(1 + z_s)R_0/c$ of the lamp post model and verified that a uniform magnification leads to no change in the mean delays.

We found no simple relationships between the mean magnification and the effect on the time delay. The only relatively clean trend is that the lamp post delays tend to be positive for low mean magnifications and negative for high mean magnifications. This is likely explained by the need to strongly magnify only the central regions of the disc in order to produce negative lamp post delays. The inclination component of the delay shows no strong trends with the mean magnifications.

Table 2 summarizes the mean and dispersion of the delay differences between images based on randomly drawing a large number of delays from the delay distributions of the respective images. Since the mean total delays for the individual images are non-zero, the mean of the delay differences is also not zero. These non-zero means represent a bias in the delays between the images that cannot be removed simply by monitoring the lens for a long period of time. The dispersion of the delay differences about this mean represents an additional scatter introduced into a time delay between two images, which can be eliminated by monitoring the lens of a long time period. In producing Table 2, we simply used the same disc geometry for each image. In reality, the PA of the disc relative to the magnification pattern of the other images is determined once it is set for the first image to the extent that the orientation of the model shear for each image is well constrained.
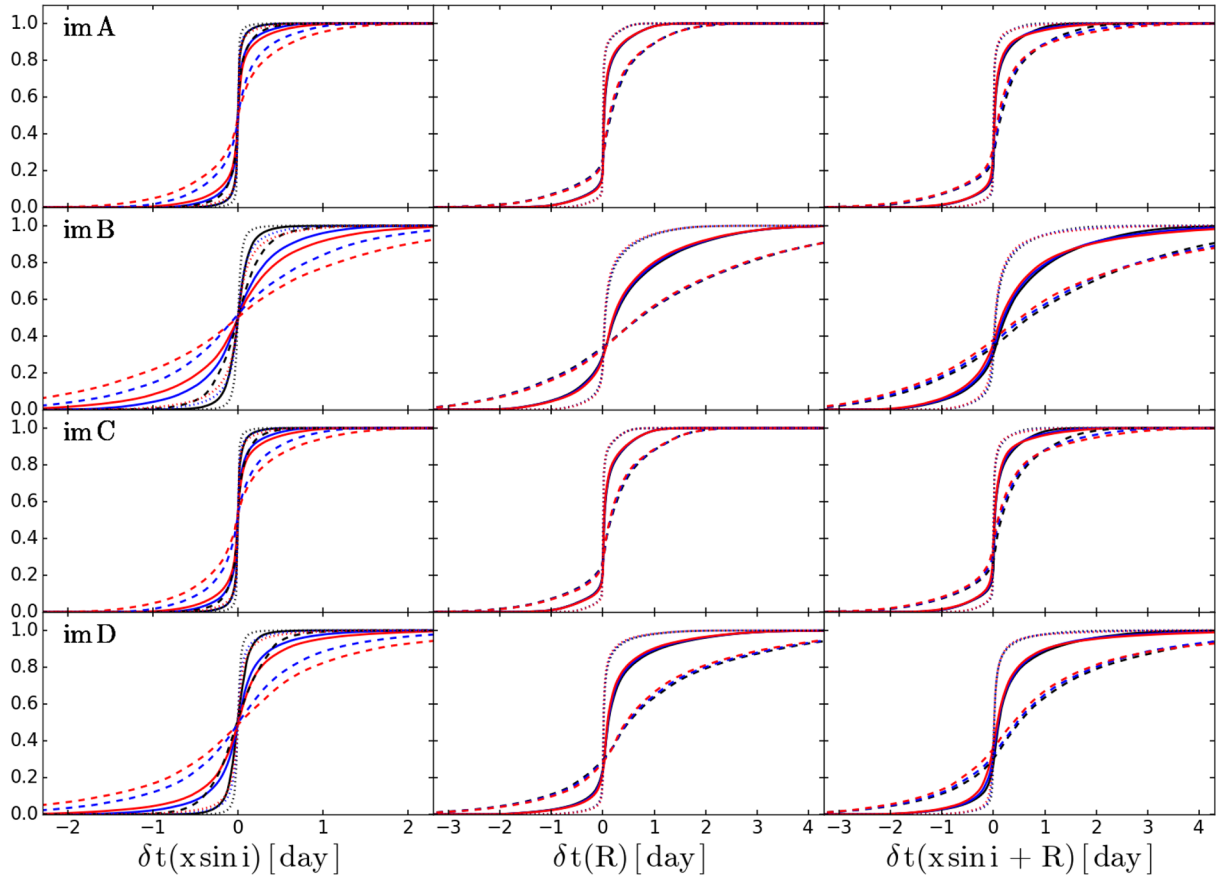
Figure 8. Same as Fig. 7, but for HE 0435−1223.

As a final illustration of microlensing effect on time delays, we created examples of microlensed quasar light curves including these effects. We used the damped random walk (DRW) model, which has been shown to capture quasar variability relatively well (Kelly, Bechtold & Siemiginowska 2009; Kozlowski et al. 2010; MacLeod et al. 2010), to generate the driving light curve $f(t)$. The driving light curve is modelled with a time-scale $\tau = 90$ d and a fractional variability of 15 per cent. This damping time τ is shorter than typical of quasars in order to make it easier to visualize the microlensing effects. These choices are simply made to illustrate the effects. Neither the choice of the DRW model nor the specific DRW parameters are important to our conclusions, as with the neglect of any higher order, non-linear contributions in the temperature variability model of equations (8) and (9).

The contribution from any point on the disc lags the driving light curve by $t_{lag} = (1 + z_s)(R - x \sin i)/c$, with a flux contribution of $f(t - t_{lag})G(\xi)$. This is then weighted either by a constant in the absence of microlensing or a magnification pattern when microlensing is present, resulting in a snapshot of the disc brightness. Repeating this as a function of time produces a set of evolving maps of the disc brightness, from which one can generate the observed light curve.

Fig. 10 shows four examples of light curves (LC1–LC4) spanning 120 d for image A of RXJ 1131−1231. The disc size is set to R_0. We show two examples for a face-on disc (LC1, LC2) and two examples for an inclined disc (LC3, LC4 with PA = 45° and $i = 30°$), where the disc positions are indicated in Fig. 4 for the latter two cases. The predicted mean shifts based on equation (10) are given in Table 3. If we shift the microlensed light curves by this delay, they match the input light curves with some small differences in structure due to the

microlensing. It is important to note that these changes in the light-curve structures are not due to any movement of the quasar relative to the magnification pattern, but are instead due to changes in the disc surface brightness with time that are differentially weighted by the fixed microlensing magnification pattern.

We next used the AGN lag estimation algorithm JAVELIN (Zu, Kochanek & Peterson 2011) to estimate the lags between the 'micro' and 'nomicro' light curves for the example light curves in Fig. 10. We assumed a generic 5 per cent fractional uncertainty and treated the 'nomicro' light curves as the driving light curve and fit for the lag of the 'micro' light curves. The median lags and their 68 per cent uncertainties are shown in Table 3. We see that the mean lags predicted by equation (10) agree well with the lags determined from the model light curves. As with the specifics in generating the light curves, JAVELIN is simply used for convenience. Any other lag estimation method (e.g. simple cross-correlation) would find the same result.

4 DISCUSSION AND CONCLUSION

Using both simple models and full simulations, we have shown that microlensing leads to perturbations in time delays on the scale of the light-crossing time of the quasar disc, of the order of ∼ days. Although the accretion disc is held fixed in this work, these delays will vary with time as the observer, source, lens and stars in the lens move relative to one another. The time-scales for changes are summarized in Mosquera & Kochanek (2011). Because the optical depth to microlensing for lensed images is almost unity, these time
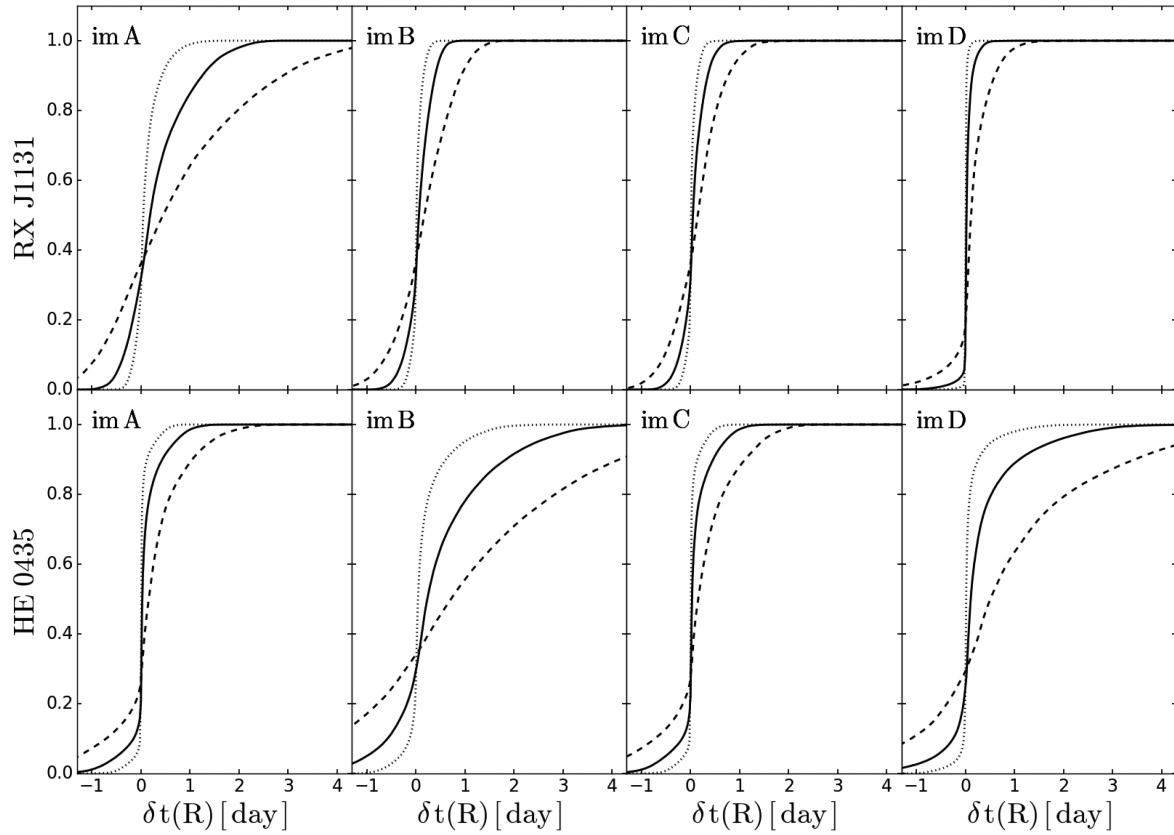
Figure 9. Cumulative distributions of the mean delays for a face-on disc. The top row is for RXJ 1131−1231 and the bottom row is for HE 0435−1223. The columns refer to the four lensed images. The disc PA does not matter for a face-on disc. The different line styles refer to source sizes of $0.5R_0$ (dotted), R_0 (solid) and $2R_0$ (dashed).

Table 2. The mean (dispersion) of the microlensing time delay differences between image pairs.

Lens	Size	PA (°)	i (°)	$B-A$ (d)	$C-A$ (d)	$D-A$ (d)	$C-B$ (d)	$D-B$ (d)	$D-C$ (d)
RXJ 1131−1231	$0.5R_0$	0	0	− 0.08 (0.27)	− 0.08 (0.27)	− 0.10 (0.25)	− 0.00 (0.15)	− 0.02 (0.11)	− 0.02 (0.11)
	−	0	30	− 0.08 (0.27)	− 0.09 (0.27)	− 0.10 (0.26)	− 0.00 (0.15)	− 0.02 (0.12)	− 0.02 (0.11)
	−	45	30	− 0.08 (0.30)	− 0.08 (0.30)	− 0.10 (0.28)	− 0.00 (0.17)	− 0.02 (0.13)	− 0.02 (0.12)
	−	90	30	− 0.07 (0.34)	− 0.08 (0.33)	− 0.09 (0.31)	− 0.00 (0.18)	− 0.02 (0.14)	− 0.02 (0.13)
	R_0	0	0	− 0.25 (0.68)	− 0.27 (0.67)	− 0.29 (0.64)	− 0.01 (0.34)	− 0.04 (0.28)	− 0.02 (0.27)
	−	0	30	− 0.25 (0.68)	− 0.27 (0.68)	− 0.29 (0.65)	− 0.01 (0.35)	− 0.04 (0.29)	− 0.02 (0.28)
	−	45	30	− 0.24 (0.74)	− 0.26 (0.74)	− 0.28 (0.71)	− 0.01 (0.38)	− 0.04 (0.32)	− 0.02 (0.30)
	−	90	30	− 0.24 (0.83)	− 0.25 (0.81)	− 0.27 (0.78)	− 0.01 (0.42)	− 0.04 (0.35)	− 0.02 (0.33)
	$2R_0$	0	0	− 0.56 (1.57)	− 0.61 (1.54)	− 0.60 (1.51)	− 0.04 (0.77)	− 0.03 (0.71)	0.01 (0.65)
	−	0	30	− 0.57 (1.57)	− 0.61 (1.55)	− 0.61 (1.53)	− 0.05 (0.78)	− 0.03 (0.74)	0.01 (0.68)
	−	45	30	− 0.57 (1.72)	− 0.61 (1.68)	− 0.61 (1.66)	− 0.04 (0.85)	− 0.03 (0.79)	0.01 (0.72)
	−	90	30	− 0.58 (1.88)	− 0.62 (1.85)	− 0.61 (1.82)	− 0.04 (0.93)	− 0.04 (0.86)	0.00 (0.78)
HE 0435−1123	$0.5R_0$	0	0	0.12 (0.42)	0.00 (0.20)	0.05 (0.31)	− 0.12 (0.42)	− 0.07 (0.48)	0.05 (0.31)
	−	0	30	0.12 (0.43)	0.00 (0.21)	0.05 (0.31)	− 0.13 (0.43)	− 0.07 (0.49)	0.05 (0.31)
	−	45	30	0.12 (0.47)	0.00 (0.23)	0.05 (0.35)	− 0.12 (0.48)	− 0.07 (0.54)	0.05 (0.35)
	−	90	30	0.11 (0.52)	0.00 (0.25)	0.05 (0.39)	− 0.11 (0.52)	− 0.07 (0.60)	0.05 (0.39)
	R_0	0	0	0.38 (1.06)	0.00 (0.47)	0.21 (0.80)	− 0.37 (1.05)	− 0.17 (1.24)	0.20 (0.80)
	−	0	30	0.38 (1.07)	0.00 (0.49)	0.20 (0.81)	− 0.38 (1.07)	− 0.17 (1.25)	0.20 (0.82)
	−	45	30	0.37 (1.16)	0.00 (0.54)	0.20 (0.91)	− 0.37 (1.17)	− 0.17 (1.38)	0.19 (0.91)
	−	90	30	0.36 (1.28)	0.00 (0.59)	0.18 (1.01)	− 0.35 (1.28)	− 0.17 (1.52)	0.19 (1.02)
	$2R_0$	0	0	0.83 (2.38)	0.01 (1.08)	0.65 (2.00)	− 0.83 (2.38)	− 0.17 (2.92)	0.65 (2.01)
	−	0	30	0.85 (2.42)	0.00 (1.10)	0.65 (2.03)	− 0.83 (2.42)	− 0.19 (2.96)	0.65 (2.04)
	−	45	30	0.85 (2.64)	0.01 (1.21)	0.64 (2.24)	− 0.83 (2.64)	− 0.20 (3.25)	0.64 (2.25)
	−	90	30	0.85 (2.87)	0.00 (1.32)	0.61 (2.48)	− 0.84 (2.89)	− 0.23 (3.57)	0.62 (2.50)
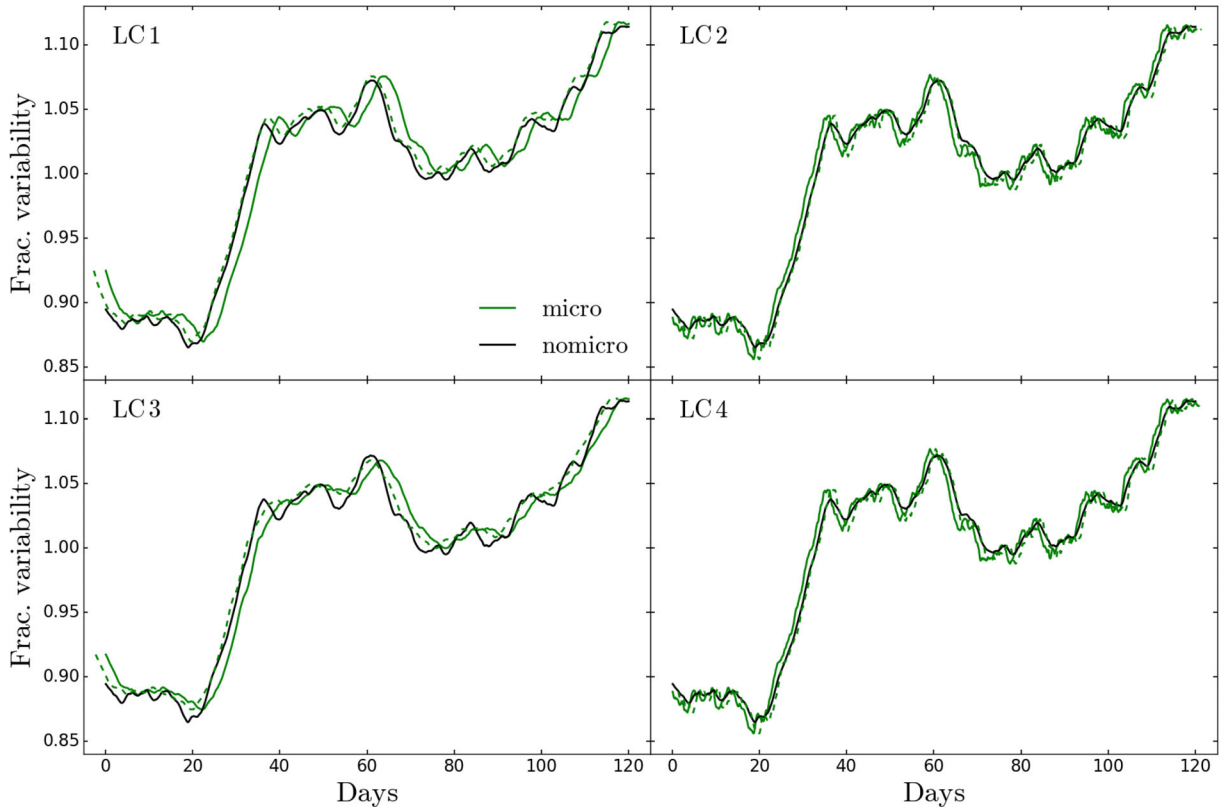
Figure 10. Example light curves for image A of RXJ 1131−1231 at randomly selected points in the map. The top panel shows two light curves for a face-on disc, while the bottom panel shows two light curves for the $i = 30°$ inclined disc at PA = 45°. The locations used for the inclined disc models are marked as 'LC3' and 'LC4' in Fig. 4. The 'nomicro' light curves in black correspond to no microlensing, while the 'micro' light curves in green include the effects of microlensing. The dashed lines show the effect of removing the predicted mean delays (Table 3). Even with the mean delays removed, the light curves are not identical because microlensing weights the temperature variation of the disc differently than a uniform weighting. The 'micro' light curves are ahead of the 'nomicro' light curves (i.e. observed at later times) when the lag is positive and vice versa.

Table 3. JAVELIN lags of example light curves.

LC	$\langle \delta t \rangle$ (d)	JAVELIN (d)
1	2.73	$2.88^{+0.42}_{-0.43}$
2	−1.32	$-1.22^{+0.39}_{-0.38}$
3	2.34	$2.30^{+0.51}_{-0.47}$
4	−1.14	$-1.07^{+0.37}_{-0.38}$

delay perturbations should be present to varying degrees in all lensed quasars.

We have been very conservative in illustrating the amplitude of the microlensing effect, scaling the disc size R_0 to a standard thin disc model with an Eddington ratio of $L/L_E = 0.1$. Typical quasars probably have higher Eddington ratios (see, e.g. Kollmeier et al. 2006), while both microlensing (e.g. Morgan et al. 2010; Mosquera & Kochanek 2011) and ongoing continuum reverberation mapping studies (e.g. Shappee et al. 2014; Fausnaugh et al. 2016) find that the accretion discs are two to four times larger than predicted by the thin disc theory. Hence, even our $2R_0$ models may still be underestimating the overall effect. Particularly for face-on discs, the effect will also depend on the quasar variability model.

The first consequence of this new effect is that the uncertainty in a lens time delay now has an additional contributor, $\sigma_\mu \sim$ days. Ignoring the lens galaxy, the two traditional sources of error are measurement error in the time delay ($\sigma_{\delta t}$) and fluctuations in the surface density along the LOS (σ_{los}). Unless the microlensing delays

can be determined, there is no need for time delay measurement errors that are significantly smaller, $\sigma_{\delta t} \ll \sigma_\mu$. This is analogous to two-image lenses where there is no point in measuring delays significantly more accurately than the limit set by the contribution from the cosmic variance in the density along the LOS, $\sigma_{\delta t} \ll \sigma_{los} \Delta t$. This microlensing effect also likely explains why repeated delay measurements of lensed quasars still vary by more than their estimated errors.

The microlensing delay effect is an absolute, rather than fractional, error. Therefore, it is more important for the short delays common in four-image lenses (due to the high degree of symmetry) such as the two lenses investigated here, while it will matter less for long delays. For example, the longest delay in HE 0435−1123 is approximately $\Delta t \simeq 14$ d, so a $\sigma_\mu = 1$ d contribution from microlensing represents a 7 per cent floor to the utility of this lens for cosmology. The longest delay in RXJ 1131−1231 is $\Delta t \simeq 91$ d, and such a microlensing effect represents a fractional error of only 1 per cent that is comparable to the effects of large-scale structure. Lenses with long time delays, which tend to be two-image lenses, are therefore strongly favoured for obtaining measurements of cosmological time delays. Unfortunately, two-image lenses supply fewer model constraints on the structure of the lens galaxy. Tagore et al. (2017) also showed that two image lenses will produce the most biased estimates of H_0 from time delays, while cruciform quads have the lowest biases. The presence of microlensing effects may well revise this conclusion, as cruciform lenses with short time delays will be strongly limited by the effects of microlensing delays. Since

the microlensing delay is on the scale of the accretion disc size $R_0 \propto M_{BH}^{2/3}(L/L_E)^{1/3}$ (equation 5), lenses with lower mass black holes and shorter disc light-crossing times are also preferred.

The microlensing delays also affect searches for substructures in lens galaxies using time delay anomalies in lensed quasars, also known as millilensing. Depending on the properties of the subhalo, substructures are thought to introduce time delay perturbations of the order of fraction of a day (Keeton & Moustakas 2009). The substructure perturbations can be investigated through measurements of time delay ratios, which are insensitive to LOS structures and less sensitive to degeneracies due to the radial mass profile of the primary lens. Particularly with the biases produced by the mean delay shifts seen for microlensing of the lamp post variability model, this new microlensing effect may make the use of delay anomalies to search for substructures problematic.

In addition to being an important new systematic problem for time delay cosmology, this effect may be a boon to quasar microlensing studies. In theory, microlensing probes the size of the source (R_0 or equivalent), the mean mass of the microlensing stars $\langle M_* \rangle$ and the effective velocity v_e of the source relative to the magnification patterns. The mean stellar mass determines the typical Einstein radius $R_E \propto \langle M_* \rangle^{1/2}$, and the effective velocity is a combination of the motion of the observer, the microlensing stars and the peculiar velocities of the lens and the source. Unfortunately, the only observable with physical units is the time-scale of the microlensing variability $t_E \propto R_E/v_e$, which is a degenerate combination of the mean *Einstein* radius and the effective velocity. This means that one must use prior estimates for one of the three variables of interest (R_0, $\langle M_* \rangle$ and v_e) in order to constrain the other two. Traditionally, we have constrained the peculiar velocities (e.g. Poindexter, Morgan & Kochanek 2008; Dai et al. 2010; Morgan et al. 2010; Mosquera et al. 2013) while most other groups have assumed a mean microlens mass.

The microlensing time delay effect provides a new observable with units that are directly related to the size of the emission region, R_0. Measuring the effect has the potential of eliminating the need for (strong) priors in microlensing analyses. For any particular image, the effect depends on the disc size and inclination, but the strong dependence of the effect on the inclination of the disc and its orientation relative to the caustic networks created by the tangential magnification suggests that it may be possible to disentangle the two effects, particularly for four-image lenses. The projected shape and orientation of the disc is fixed on the sky, but the orientation of the caustic networks rotates from image to image, so the differences in the microlensing time delay effects between the images should strongly constrain both variables.

ACKNOWLEDGEMENTS

REFERENCES

Astropy Collaboration et al., 2013, A&A, 558, A33
Birrer S., Amara A., Refregier A., 2016, J. Cosmol. Astropart. Phys., 8, 020
Blandford R., Narayan R., 1986, ApJ, 310, 568
Bonvin V., Tewes M., Courbin F., Kuntzer T.; Sluse D.; Meylan G., 2016, A&A, 585, A88
Bonvin V. et al., 2017, MNRAS, 465, 4914
Burud I. et al., 2002, A&A, 391, 481
Cackett E. M., Horne K., Winkler H., 2007, MNRAS, 380, 669
Collier S. J. et al., 1998, ApJ, 500, 162
Dai X., Kochanek C. S., Chartas G., Kozlowski S., Morgan C. W., Garmire G., Agol E., 2010, ApJ, 709, 278
Dexter J., Agol E., 2011, ApJ, 727, L24
Dobler G., Fassnacht C. D., Treu T., Marshall P., Liao K., Hojjati A., Linder E., Rumbaugh N., 2015, ApJ, 799, 168
Fassnacht C. D., Xanthopoulos E., Koopmans L. V. E., Rusin D., 2002, ApJ, 581, 823
Fausnaugh M. M., Denney K. D., Barth A. J. et al., 2016, ApJ, 821, 56
Goicoechea L. J., 2002, MNRAS, 334, 905
Gould A., Miralda-Escudé J., 1997, ApJ, 483, L13
Granot J., Schechter P. L., Wambsganss J., 2003, ApJ, 583, 575
Greene Z. S. et al., 2013, ApJ, 768, 39
Keeton C. R., Moustakas L. A., 2009, ApJ, 699, 1720
Keeton C. R., Zabludoff A. I., 2004, ApJ, 612, 660
Kelly B. C., Bechtold J., Siemiginowska A., 2009, ApJ, 698, 895
Kochanek C. S., 1993, MNRAS, 261, 453
Kochanek C. S., 2002, ApJ, 578, 25
Kochanek C. S., 2004, ApJ, 605, 58
Kochanek C. S., 2006, in Meylan G., Jetzer P., North P., eds, Saas-Fee Advanced Course 33: Gravitational Lensing: Strong, Weak and Micro. Springer, Berlin, p. 91
Kollmeier J. A. et al., 2006, ApJ, 648, 128
Kozłowski S. et al., 2010, ApJ, 708, 927
Krolik J. H., Horne K., Kallman T. R., Malkan M. A., Edelson R. A., Kriss G. A., 1991, ApJ, 371, 541
Kundić T. et al., 1997, ApJ, 482, 75
Liao K. et al., 2015, ApJ, 800, 11
McCully C., Keeton C. R., Wong K. C., Zabludoff A. I., 2017, ApJ, 836, 141
MacLeod C. L. et al., 2010, ApJ, 721, 1014
Morgan C. W., Kochanek C. S., Morgan N. D., Falco E. E., 2010, ApJ, 712, 1129
Mosquera A. M., Kochanek C. S., 2011, ApJ, 738, 96
Mosquera A. M., Kochanek C. S., Chen B., Dai X., Blackburne J. A., Chartas G., 2013, ApJ, 769, 53
Poindexter S., Morgan N., Kochanek C. S., 2008, ApJ, 673, 34
Press W. H., Rybicki G. B., Hewitt J. N., 1992, ApJ, 385, 404
Refsdal S., 1964, MNRAS, 128, 307
Schechter P. L. et al., 2003, ApJ, 584, 657
Schild R. E., 1990, AJ, 100, 1771
Schneider P., 1985, A&A, 143, 413
Schneider P., Sluse D., 2013, A&A, 559, A37
Shakura N. I., Sunyaev R. A., 1973, A&A, 24, 337
Shappee B. J. et al., 2014, ApJ, 788, 48
Sluse D. et al., 2003, A&A, 406, L43
Starkey D. et al., 2017, ApJ, 835, 65
Suyu S. H., Marshall P. J., Auger M. W., Hilbert S., Blandford R. D., Koopmans L. V. E., Fassnacht C. D., Treu T., 2010, ApJ, 711, 201
Suyu S. H. et al., 2014, ApJ, 788, L35
Tagore A. S., Barnes D. J., Jackson N., Kay S. T., Schaller M., Schaye J., Theuns T., 2017, MNRAS, preprint (arXiv:1706.07733)
Tewes M., Courbin F., Meylan G., 2013a, A&A, 553, A120
Tewes M. et al., 2013b, A&A, 556, A22
Treu T., Marshall P. J., 2016, A&AR, 24, 11
Walsh D., Carswell R. F., Weymann R. J., 1979, Nature, 279, 381
Wambsganss J., 2006, in Meylan G., Jetzer P., North P., eds, Saas-Fee Advanced Course 33: Gravitational Lensing: Strong, Weak and Micro. Springer, Berlin, 453
Wanders I. et al., 1997, ApJS, 113, 69
Wisotzki L., Schechter P. L., Bradt H. V., Heinmüller J., Reimers D., 2002, A&A, 395, 17
Wyithe J. S. B., Loeb A., 2002, ApJ, 577, 615
Yonehara A., 1999, ApJ, 519, L31
Zu Y., Kochanek C. S., Peterson B. M., 2011, ApJ, 735, 80

This paper has been typeset from a TeX/LaTeX file prepared by the author.